RADIATIVE TRANSFER MODELING FOR QUANTIFYING LUNAR SURFACE MINERALS, PARTICLE SIZE AND SUBMICROSCOPIC IRON (SMFe)

Shuai Li

Submitted to the faculty of the University Graduate School
in partial fulfillment of the requirements
for the degree
Master of Science
in the Department of Earth Sciences,
Indiana University

November 2011

Accepted by the Faculty of Indiana University, in partial fulfillment of the requirements for the degree of Master of Science.

_____
Lin Li, Ph.D., Chair

Master's Thesis
Committee

_____
Kathy Licht, Ph.D.

_____
R. Jeffery Swope, Ph.D.

ACKNOWLEDGEMENTS

First and foremost, I would like to thank my graduate committee, especially my graduate chair, Dr. Lin Li. It's him who leads me to a new research area: planetary remote sensing. In the last two years, I have learned a lot from him. Under his guidance, I made significant improvement for the implementation of radiative transfer model.

I appreciate Dr. Kathy Licht and Dr. R. Jeffery Swope for their fruitful suggestions and comments in preparing and improving the thesis manuscript.

I am also thankful to Dr. Kaishan Song, Dr. Tingting Zhang, Linhai Li, Zuchuan Li, Ying Sun, Kun Shi and Dawei Liu. I spent most of my time with them. It's them who make me have a wonderful time here.

I also want to thank all the faculty, staff and students in our department for their any kind of assistant. It will be one of my best experiences for the past two years.

I appreciate the financial aid from Indiana University – Purdue University Indianapolis.

ABSTRACT

Shuai Li

RADIATIVE TRANSFER MODELING FOR QUANTIFYING LUNAR SURFACE MINERALS, PARTICLE SIZE AND SUBMICROSCOPIC IRON (SMFe)

The main objective of this work is to better quantify lunar surface minerals (agglutinate, clinopyroxene, orthopyroxene, plagioclase, olivine, ilmenite, and volcanic glass), particle sizes and the abundance of SMFe from the lunar soil characterization consortium (LSCC) dataset with our improved model based on Hapke's radiative transfer theory. The model is implemented for both forward and inverse modeling. Hapke's radiative transfer theory is implemented in the inverse model means Newton's method and least squares are jointly used to solve nonlinear questions rather than commonly used look-up Table (LUT). Although the effects of temperature and surface topography are incorporated into the implementation to improve the model performance for application of lunar spacecraft data, these effects cannot be extensively addressed in the current work because of the use of lab measured reflectance data. Our forward radiative transfer model (RTM) results show that the correlation coefficients between modeled and measured spectra are over 0.99. For the inverse model, the distribution of the calculated particle sizes is all within their measured range. The

range of modeled SMFe for highland samples is 0.01% - 0.5 % and for mare samples is 0.03% - 1 %. The linear trend between SMFe and ferromagnetic resonance (Is) for all the LSCC samples is consistent with laboratory measurements. For quantifying lunar mineral abundances, the results show that the R-squared for the training samples (Is/FeO <= 65) are over 0.65 with plagioclase having highest correlation (0.94) and pyroxene the lowest (0.68). In the future work, the model needs to be improved for handling more mature lunar soil samples.

Lin Li, Ph.D., Chair

TABLE OF CONTENTS

LIST OF TABLES

LIST OF FIGURES

I. INTRODUCTION

Mineral compositions and physical properties of lunar regolith are the basis for investigates of the Moon such as space weathering processes, crustal structure and the 'magma ocean' hypothesis. On the lunar surface, variations of lunar soils in minerals and physical properties (e.g., particle size, porosity, and maturity) indicate how space weathering works on lunar soils [*Mckay et al., 1974; Noble et al., 2001; Starukhina and Shkuratov, 2001; Taylor et al., 2003, 2010; Anand et al., 2004*]. One of the most important indicators for the maturity is the abundance of submicroscopic iron (SMFe) that is generated under space weathering. Beneath the surface, lunar crustal structure can be characterized by examining the mineralogy of ejecta from craters penetrating through the lunar crust [*Taylor, 1979; Pieters, 1986; Pieters et al., 1997; Tompkins and Pieters, 1999; Cahill et al., 2009*]. The mineral distribution from the lunar surface to interior can provide evidence for the 'magma ocean' hypothesis that is used to address the formation and evolution of lunar crust [*Wood, 1975; Solomon and Longhi, 1977; Longhi, 1978; Warren, 1985, 1990; Pieters 1993b; Tanton et al., 2002*].

Dominant minerals of the lunar soil are agglutinate (aggregates of smaller lunar soil particles), plagioclase, pyroxene (clinopyroxene, orthopyroxene), olivine, ilmenite, and volcanic glasses (black, orange, etc.) [e.g., *Heiken et al.,*

1991]. Formation of agglutinate is probably by the melting and mixing produced by bombardment of lunar regolith. Longer time exposure for weathering results in the increase in agglutinate. Thus abundances of agglutinate are generally higher in the highland than in the mare. On average, 75-95% of plagioclase in the oldest lunar crust is probably produced by 'Magma Ocean'; however this is still debated [e.g., *Warren, 1985, Pieters et al., 1993a*]. Plagioclase is wildly distributed in the highland area. Pyroxene, olivine, and ilmenite are materials from deeper lunar crust or its mantle [*Taylor, 1979; Heiken et al., 1991; Tompkins and Pieters, 1999*]. They were ejected during lunar volcanisms or exposed by large impacts which penetrate through lunar crust [e.g., *Pieters and Englert, 1993, Heiken et al., 1991*]. Volcanic glasses are also products of volcanoes on the Moon. Hence, pyroxene, olivine, ilmenite and volcanic glasses are rich in lunar lowlands where volcanoes erupt easily to the surface and the crust can be penetrated by meteorite impacts.

The realistic approach to mapping lunar surface minerals is by applying remote sensing image data. Dominant minerals of the lunar surface exhibit diagnostic absorption features between 600 nm and 2500 nm [*Pieters and Englert, 1993*]. Plagioclase shows a broad weak absorption near 1250 nm (Figure 1), which is caused by Fe^{2+} [*Adams and Goulland, 1978*]. Olivine exhibits a wide absorption bands centered at 1050 nm (Figure 1). Clinopyroxene has two

absorption bands near1000 nm and 2100 nm. Orthopyroxene are similar to clinopyroxene (Figure 1) near 900 nm and 2000 nm. Ilmenite has very weak absorption features (Figure 1). Agglutinate exhibit two diagnostic absorption bands near 1000 nm and 1900 nm. Black glass (one of volcanic glasses) shows higher absorption in shorter wavelengths (< 1000 nm) than longer wavelengths and has two absorption bands near 950 nm and 2000 nm.

Space weathering has significant influence on the spectral absorption features of lunar surface minerals. Space weathering and H_2 on the lunar surface provide a reducing environment. Typical change in lunar regolith over time is that Fe^{2+} is reduced to Fe^0 (also called submicroscopic iron or nanophase iron), which contributes to the ferromagnetic resonance intensity (Is, caused by single domain SMFe). More agglutinate will be generated under longer time weathering. All mineral particle sizes become smaller and smaller due to bombardment, solar wind and meteoroid impacts. If Fe^0 is contained in these minerals, their spectra will become redder, darker, and lose spectral contrast [*Heiken et al., 1991; Lucey et al., 1995; Starukhina and Shkuratov, 2001; Noble et al., 2001; Taylor et al., 2010*]. As the amount of agglutinate increases, its spectra will lose spectral contrast [*Heiken et al., 1991; Taylor et al., 2003, 2010*]. Particle size of minerals has a negative relationship with their reflectance intensity [*Mackey et al., 1974; Noble et al., 2001; Starukhina and Shkuratov, 2001; Taylor et al., 2003, 2010]*.

Thus, mineralogy and space weathering both affect spectral features of lunar regolith.

Based on mineral absorption properties of lunar regolith, lunar global mineral mapping and lunar regolith physical properties can be investigated with remote sensing images (such as: Clementine ultraviolet-visible-near infrared images). Although a variety of data analysis techniques for these quantitative compositional analyses have been described in literature, the commonly used approach can be classified into two groups depending on whether 'ground truth' data are required. The method requiring the ground truth data for calibration includes Gaussian model (GM), modified Gaussian model (MGM) [e.g., *Sunshine et al., 1990; Sunshine and Pieters, 1993; Noble et al., 2006; Tsuboi et al., 2010*], multiple linear regression model (MLR) [*Shkuratov et al., 2003, 2005*], principal component regression (PCR) [*Pieters et al., 2002*], partial least squares (PLS) regression [*Li, 2006*], genetic algorithm - partial least squares (GA-PLS) [*Li and Li, 2010*] and artificial neural network (ANN) [*Korokhin et al., 2008*]. Of these approaches, GM and MGM are suitable for the use with hyperspectral data, while the remaining methods can be applied to both hyper- and multi-spectral data with ANN being a nonlinear model and others (MLR, PCR, PLS, and GA-PLS) being linear. Current methods that do not require ground truth data are spectral mixture analysis (SMA) and RTM with RTM having the advantages over SMA in that

RTM takes physical factors (e.g., the particle size, the maturity, and the porosity) into account (see section 2 for details). To evaluate these methods, terrestrial data can be used.

There are two kinds of RTM dominantly used by scientists [*Hapke, 1981; Shkuratov et al., 1999*]. Since Hapke's model has advantages over other similar theories, it is a most commonly used one [*Clark and Roush, 1984; Mustard and Pieters, 1987, 1989; Clark et al., 2001; Lucey, 2004; Wilcox et al., 2006; Lawrence and Lucey, 2007; Cahill and Lucey, 2007; Denevi et al., 2008; Cahill et al., 2009; Li and Li, 2010*] (see section 2.7 for details).

In this study, we present a new implementation of the Hapke model where instead of commonly used LUT, Newton's theory and the least square optimization method are used to solve non-linear equations for estimating the abundance of agglutinate, plagioclase, clinopyroxene, orthopyroxene, olivine, ilmenite and volcanic glasses; the same approach is also used for derivation of the imaginary coefficient (k) of mineral end-members' optical constants. Moreover, spectral effects of space weathering, topography and temperature are explicitly accommodated in this implementation. The implemented model is assessed in forward and inverse modes with the LSCC dataset including the highland and mare samples. In the forward RTM, the reflectance spectra of the LSCC soil samples are modeled and in the inverse RTM, the abundance of mineral, SMFe

and particle size are derived and compared with the measured values to evaluate the performance of RTM implemented in this study. If this implementation of the Hapke model is proved to be robust and efficient, it can be applied to lunar hyperspectral remote sensing data (e.g., Moon Mineral Mapper (M^3) data) acquired recently. This will be the only model that can take both mineralogy and physical factors into account for mapping lunar surface minerals.

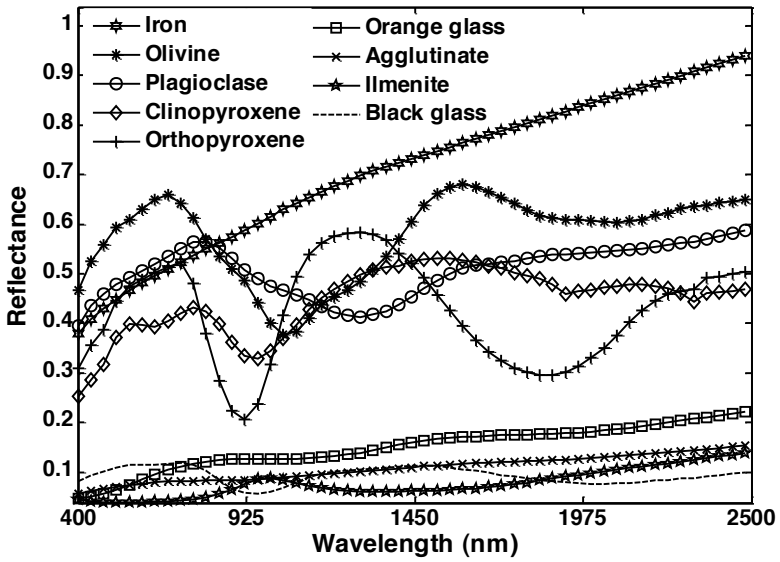

Figure 1. Reflectance spectra of major mineral endmembers, the spectrum of orthopyroxene is the average of the three same minerals and the spectrum of volcanic glass is the average of the two corresponding samples listed in Table 1.

II. LITERATURE REVIEW

In this section, commonly used methods in literatures for quantifying lunar surface minerals and lunar soil physical properties are described in detail.

2.1. Gaussian model (GM) and modified Gaussian model (MGM)

GM and MGM can be used to deconvolve an absorption band of spectra into a modified Gaussian shape that can be described by three terms: absorption center, absorption strength, and absorption bandwidth. Distinct absorption centers indicate different minerals. Variation of absorption strength indicates high or low abundances of certain minerals.

GM and MGM are based on two assumptions. They are: absorption bands in the VIS-NIR region are inherently Gaussian in shape, and the electronic and vibrational processes that cause absorption must be randomly distributed. Then, in Gaussian model, absorption bands can be described in mathematical formula:

$$e(x) = a \bullet \exp\left[\frac{-(x-\mu)^2}{2\sigma^2}\right] \qquad (1)$$

$e(x)$ is used to describe the absorption feature or called absorption energy. x is wavelength, μ is the absorption center, σ is absorption width, a is absorption strength. After deconvolution of characteristic absorption bands of a spectrum, mineral species can be determined by absorption centers of these

Gaussian shapes. Mineral abundances can be quantified via absorption strength of these Gaussian shapes.

Using GM, a single absorption band cannot be deconvolved to one Gaussian distribution, which bring trouble to explain these extra deconvolved Gaussian distributions. Plus, energies of electronic transition absorptions are a function of the distortion and the average ligand-ion bond length of the crystal field site, which means energies of these absorptions are not Gaussian. *Sunshine et al.* [1990] proposed that the average bond length is randomly distributed. And the absorption energy (f) has a relationship with the average bond length (l):

$$f \propto l^n \qquad (2)$$

A modified Gaussian distribution of absorption energy ($h(x)$) was described as:

$$h(x) = a \bullet \exp\left[\frac{-(x^n - \mu^n)^2}{2\sigma^2}\right] \qquad (3)$$

Sunshine et al. [1990] gave an empirical value for n: $n \approx -1$. In addition, they mentioned that the continuum of the reflectance spectrum is caused by numerous factors including first surface reflectance, multiple scattering, wings of strong ultraviolet absorptions, and absorptions from materials with constant spectral signatures. In order to eliminate spectral effects of all these factors, the deconvolved Gaussian distributions are superimposed onto the continuum.

Sunshine and Pieters [1993] applied MGM to estimate pyroxene abundances from natural and laboratory pyroxene mixtures. *Noble et al.* [2006] applied MGM to estimate abundances of dominant minerals (agglutinate, pyroxene, plagioclase, and olivine) of lunar soil samples with the lunar soil characterization consortium (LSCC) dataset. In their study, continuum of the reflectance spectrum of lunar soils is considered largely caused by space weathering and is removed. However, only prediction of pyroxene had higher accuracy. In MGM, for a single absorption band, the number of Gaussians is hard to decide. *Tsuboi et al.* [2010] jointly used MGM and a cross-validation method. Relationship between root mean square error (RMSE) and Gaussian number was plotted. With the plot, where the RMSE became the least, the optimized Gaussians was selected.

In MGM, minerals with featureless spectra cannot be identified for lunar soil mineral analysis, only the prediction for pyroxene performed well [e.g., *Moroz and Arnold, 1999*]. Additionally, physical factors such as topography, particle size, and temperature cannot be taken into account. When applying MGM to planetary research, the key problem is that it is only suitable for hyperspectral data because for most planets we do not have hyperspectral data.

2.2. Vector machine and multiple linear regression (MLR)

MLR is a kind of linear regression method. In a MLR model, reflectance is commonly used as independent variables *X*. Mineral abundances are used as dependent variables *Y*. Because absorption bands in the VIS-NIR region of the lunar soil spectra are attributed to compositions (chemical and mineralogical) of lunar soils, *X* and *Y* are assumed to have a relation like:

$$Y = a_1 x_1 + a_2 x_2 + \cdots + a_n x_n + \varepsilon \qquad (4)$$

n stands for number of absorption bands used as independent variables. $a_i, i = 1,2,...,n$ are coefficients. ε is the residual. This model is not constrained by hyperspectral data.

With training samples, all coefficients $a_i, i = 1,2,...,n$ can be regressed. When new spectra data are available, mineral abundances can be estimated with the equation 4.

Shkuratov et al. [2005] applied MLR to map clinopyroxene and plagioclase of lunar surface with Clementine UVVIS images. Reflectance centered at four bands 415 nm, 750 nm, 900 nm, and 1000 nm was used. High correlation coefficients between measured and predicted mineral abundances were obtained ($r > 0.9$). However, no mapping results for other dominant minerals of lunar surface, such as: ilmenite, olivine, agglutinate and volcanic glass were published with this method.

To accommodate the non-linearity existing between lunar soil reflectance and mineral abundances, vector machine is commonly used to increase data dimensions via non-linear kernel functions. *Shkuratov et al.* [2003] jointly applied vector machine and MLR to model compositions of lunar surface with simulated SMART-1 data. Band ratios ($R_{915\ nm}$ / $R_{750\ nm}$, $R_{965\ nm}$ / $R_{750\ nm}$) and curvatures (($R_{750\ nm}$ * $R_{965\ nm}$)/ ($R_{915\ nm}$)^2) were used as kernel functions for vector machine. Only abundances of pyroxene were spectrally estimated with this method. The correlation coefficient for measured and modeled pyroxene was 0.86. *Pieters et al.* [2006] also jointly applied vector machine and MLR to estimate pyroxene and maturity from Clementine images spectra, and 6 parameters ($R_{750\ nm}$, $R_{415\ nm}$ / $R_{750\ nm}$, $R_{900\ nm}$ / $R_{750\ nm}$, R950 $_{nm}$ / $R_{750\ nm}$, $R_{1000\ nm}$ / $R_{750\ nm}$, ($R_{750\ nm}$ * $R_{1000\ nm}$) / ($R_{900\ nm}$)^2) were used. Accuracies for prediction of total pyroxene, pigeonite, augite, and agglutinate are all very high (the correlation coefficients for all these estimations are over 0.8).

Although MLR is easy to perform and is effective for estimating pyroxene and agglutinate, its performance could be largely degraded due to co-linearity. Spectral bands containing much overlapped information can be chosen as regression variables. But, for MLR, it is assumed that all regression variables are independent.

2.3. Principal component regression (PCR)

PCR is a regression method using the principal components of independent variables to replace the original independent variables. Similar to MLR, mineral abundances are used as dependent variables *Y*. But principle components of spectra are used as new independent variables *X*. Thus, in PCR, co-linearity problems between spectral bands are solved. *X* and *Y* have a relation like:

$$Y = a_1 pc_1 + a_2 pc_2 + \cdots + a_n pc_n + \varepsilon \qquad (5)$$

n is the number of principle components. $a_i, i = 1,2,...,n$ are coefficients. ε is the residual.

Pieters et al. [2002] applied PCR to estimate dominant mineral abundances of lunar soils from the LSCC data. Only prediction results for pyroxene and agglutinate had high accuracy (correlation coefficients are: 0.94, 0.8, relatively). *Li* [2006] compared PCR and PLS (see section 2.4) models to quantify lunar soil compositions from the LSCC data. PLS performed better than PCR for the prediction of chemical and mineral abundances.

In PCR model, co-linearity among spectral bands and noises existed in spectra can be removed, but the noises existed in measured mineral abundances cannot be accommodated, which will largely degrade the performance of PCR.

2.4. Partial least square (PLS)

PLS is a kind of regression methods that bears some relation to PCR. In a PLS model, eigenvectors of the independent variables are used in PLS models so that the corresponding scores (latent variables) not only explain the variance of independent variables but also have high correlation with response variables (e.g., mineral abundances), which is the advantage of PLS over PCR and other linear regression methods [e.g., *Li, 2006*]. A simplified PLS model can be performed through the process shown in Figure 2.

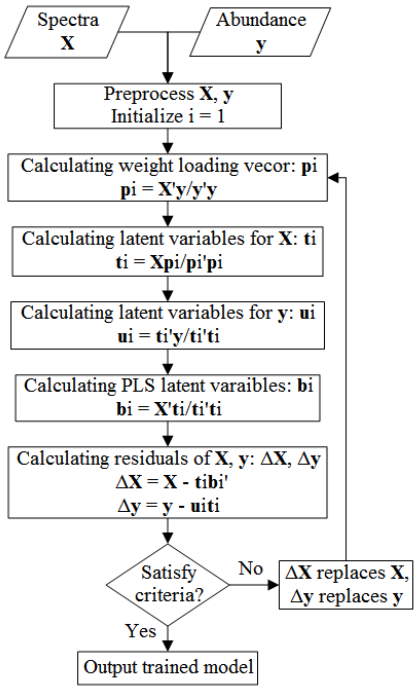

Figure 2. Flow chart of a simplified PLS model.

Criteria for the iteration can be set as: when $\Delta\mathbf{X}$ or $\Delta\mathbf{Y}$ is less than a value, calculation will stop, or the number of iterations can be set as the criteria. When the times of iteration reach a number, calculation stops. After training the model, new estimations of dependent variables can be calculated as:

$$\hat{a} = S'P'(BP')^{-1}U \qquad (6)$$

$\hat{a}$ is the estimated mineral abundance vector; $\boldsymbol{S}$ is the new spectra matrix; $\boldsymbol{P}$ is the weight loading matrix from trained PLS; $\boldsymbol{B}$ is the latent variable matrix of PLS model; $\boldsymbol{U}$ is the latent variable matrix of y.

With the LSCC dataset, PLS models exhibited a good prediction results for agglutinate (relative root mean square error (RMSE) 10.56%), pyroxene (relative RMSE 17.83%), plagioclase (relative RMSE 22.28%), and olivine (relative RMSE 23.46%) [*Li, 2006*]. However, the prediction errors of PLS for lunar surface dominant minerals are all larger than 10% [*Li, 2006*] indicates that the non-linear relationship between lunar soil spectra and lunar soil constituents cannot be modeled effectively by this method (MLR and PCR have the same problem). This results in that the accuracy for MLR, PCR and PLS is difficult to be improved. Data redundancy is another indispensable problem when performing PLS with hyperspectral data because the first latent variable of PLS is the approximation of all independent variables. However, for individual dependent variables their variations are only sensitive to some independent variables, such as

pyroxene is only sensitive to spectral bands at near 1000 nm and 2000 nm; olivine is only sensitive to spectral bands at around 1100 nm.

2.5. Genetic algorithm-partial least squares (GA-PLS)

GA is a kind of method used to search the best solutions for optimization problems through mimicking the process of natural evolution. GA is used to select the band subsets that are sensitive to variation of the mineral abundance from the whole spectral bands set. In a simplified GA model, there are five steps: encoding, initializing, evaluating with fitting function, crossover, and mutation. In a GA-PLS model, the fitting function is a simplified PLS model. The following flowchart shows how GA-PLS works (Figure 3).

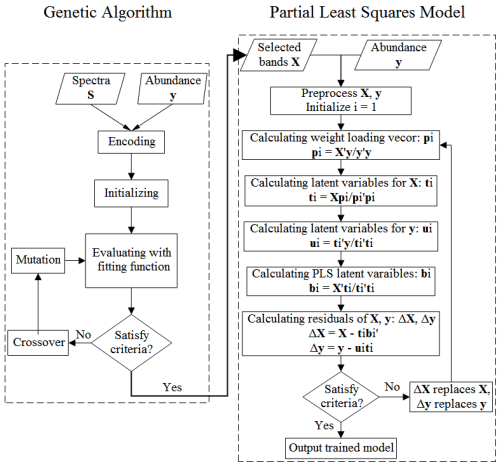

Figure 3. Flow chart of a GA-PLS model.

Li and Li [2010] used GA-PLS model to map lunar surface dominant minerals including agglutinate, pyroxene (clinopyroxene, orthopyroxene, and augite), plagioclase, olivine, ilmenite, and volcanic glasses. Mapping results for all these minerals are consistent with priori knowledge. Non-linearity can also not be accommodated effectively by GA-PLS models.

2.6. Artificial neural network (ANN)

ANN is a class of non-linear models. This kind of model is composed of many idealized layers of neurons connected by variable weights, and specified by the neuron characteristics (weights), the learning rules (transfer functions or called sigmoid functions), network interconnection geometry (different layers), and dimensionality (number of layers and neurons). ANN resembles the brain in learning and storing the knowledge [*Ripley, 1996; Bishop, 1998*]. This learning feeds back to change weights of neurons between layers to decrease errors between predicted and measured values. Once weights of neurons have been trained, ANN can be used to do prediction with new input data. Then non-linearity can be explained by sigmoid functions.

Korokhin et al. [2008] applied ANN to determine TiO_2 abundance of the lunar surface with the LSCC data, and the resultant correlation coefficient between measured and predicted TiO_2 abundance was 0.99. In spite of this good

prediction result, reliability of ANN needs further investigation because of several limitations to ANN. First, the initialization of nodes' weights is random and a large number of samples are needed for training the model to stabilize nodes' weights. However this is unrealistic for investigations of the Moon and other planets. Second, the number of neural layers and nodes has no physical meaning. It is difficult to decide how many hidden layers and hidden nodes should be put in an ANN model without the tests from a large number of training samples.

MLR, PCR, PLS, GA-PLS and ANN have two common weaknesses. One is that 'ground truth' data should cover the full range of each mineral abundance variation to achieve stable and accurate prediction results. The other is that in these models, it is hard to analyze physical properties of lunar soils such as particle size, maturity, temperature, and surface topography. As mentioned in the introduction, these factors affect lunar soil spectral features.

2.7. Spectral mixture analysis (SMA)

SMA is a method used to determine all materials that make up a pixel. In SMA models, it is assumed that the reflectance spectrum of a pixel is a linear combination of spectra of distinct components in this pixel. And the spectra of all end-members can be chosen from images. Thus, 'ground truth' data are not necessary.

$$R(\lambda) = \sum_{i=1}^{n} r(i,\lambda) f_i + e(\lambda) \qquad (7)$$

Where $R(\lambda)$ is the reflectance spectra of a pixel at wavelength λ, $r(i,\lambda)$ is the reflectance of the ith end-member at wavelength λ, f_i is the relative fraction of the ith end-member, *n* is the number of end-members in this pixel, and $e(\lambda)$ is the residual error at band λ.

SMA has been extensively applied for mineral mapping of the Earth, Moon and other planets [e.g., *Li et al., 1996; Hiroi et al., 1993; Li and Mustard, 2000; Li and Mustard, 2003*]. However, traditional SMA deconvolves each pixel with the same set of end-members, no matter whether all of these end-members are contained in this pixel. And the number of these end-members should be no more than the number of spectral bands. Multiple end-member spectral mixture analysis (MESMA), which is an extension of SMA, can overcome this limitation. In MSEMA, the number of end-members is not limited to the number of spectral bands. Though in each time of unmixing process the number of end-members should be no more than the number of spectral bands, all subsets of the whole end-member library will be calculated once. Optimized subsets of end-members will be obtained as the real constituents of the pixel. *Combe et al.* [2010] applied MSMA to extract distinct soils types of lunar surface from moon mineral mapper (M^3) data. *Li and Mustard* [2003] jointly used MESMA and Hapke' model to investigate highland contamination in lunar mare soils. Their results showed that

MESMA accommodates the compositional variation of mare soils better than SMA does. However, if there is no 'ground truth' data, it is hard to pick out pure end-members, especially with remote sensing image from the Moon and other planets.

2.8. Radiative transfer modeling (RTM)

Radiative transfer models are based on fundamental equations of radiative transfer that are commonly used to calculate how the intensity of an electromagnetic wave changes as the wave propagates through a complex medium. Radiative transfer models take into account not only mineralogy (including relative abundances) but also particle size, space weathering, temperature, topography and other physical factors. Additionally, simulation of the lunar soil reflectance spectrum with RTM is based on the optical constant of the lunar soil mineral end-members. The optical constant is the stable physical property of minerals that can be measured in laboratory. Thus, to build a RTM, no 'ground truth' data are needed.

There are two kinds of RTM dominantly used by scientists [*Hapke, 1981; Shkuratov et al., 1999*]. First is Shkuratov's theory. The following formulas are used to illuminate *Shkuratov's* theory.

$$R(n,k,S,q,\lambda) = \frac{1+\rho_b^2-\rho_f^2}{2\rho_b} - \sqrt{\left(\frac{1+\rho_b^2-\rho_f^2}{2\rho_b}\right)^2 - 1} \qquad (8)$$

R is the reflectance of the *Shkuratov' s* one-dimensional model. n is the refractive index, the real part of the optical constant. k is the absorption coefficient, the imaginary part of the optical constant. *S* is the average optical path length. *q* is the volume filled by particles in an intersecting plane or a line. λ is the wavelength. ρ_b and ρ_f are the one dimensional indicatrix for a layer of medium. ρ_b is used to describe the back scattering of light while ρ_f is to describe the forward scattering light.

In *Shkuratov's* theory all angle dependences of reflectance are ignored, which means surface topography is assumed constant [*Shkuratov et al., 1999*; *Poulet et al., 2002; Poulet and Erard, 2004*].

Second is *Hapke's* theory. Assuming that all materials in the media are mixed intimately and the particle size is much larger than the spectral wavelength, Hapke provided an approximate solution to the radiative transfer equation that describes how the intensity of an electromagnetic wave changes as the wave propagates through a complex medium [*Hapke, 1981, 1984, 1986, 2001, 2005*]. The following formulas of Hapke's theory are used for estimating lunar soil minerals in previous studies.

$$R = \frac{\omega_{ave}}{4\pi} \frac{\mu_0}{\mu_0 + \mu} \left\{ \left[1 + B(g) \right] P(g) + H(\mu_0, \omega_{ave}) H(\mu, \omega_{ave}) - 1 \right\} \qquad (9)$$

where R is the bidirectional reflectance from a smooth surface, ω_{ave} is the average single scattering albedo (SSA) of all components in the medium, μ_0 is the cosine of an incidence angle (i) ($\mu_0 = \cos(i)$), μ is the cosine of an emittance angle (e) ($\mu = \cos(e)$), and g is the phase angle; $B(g)$ is the back scattering function used to describe the opposition effect which is strong at a near zero phase angle [*Hapke, 2005*]; $P(g)$ is the phase function describing how reflected energy changes with the viewing direction changes; and $H(\mu_0, \omega_{ave}), H(\mu, \omega_{ave})$ are the H function describing the multiple scattering process. The average SSA can be computed as:

$$\omega_{ave} = \sum_i \frac{M_i \omega_i}{\rho_i d_i} \Big/ \sum_i \frac{M_i}{\rho_i d_i} \quad (10)$$

where i denotes the i^{th} component, M_i is the mass fraction, ω_i, ρ_i and d_i are the single scattering albedo, density and mean grain diameter of the i^{th} component.

Since it has advantages over other similar theories, Hapke's theory is the most commonly used one [*Clark and Roush, 1984; Mustard and Pieters, 1987, 1989; Clark et al., 2001; Lucey, 2004; Wilcox et al., 2006; Lawrence and Lucey, 2007; Cahill and Lucey, 2007; Denevi et al., 2008; Cahill et al., 2009; Li and Li, 2010*]. In previous studies, the reliability of *Hapke's* theory to simulate the reflectance spectrum of lunar soils has been demonstrated [e.g., *Clark et al.,*

2001; Lucey, 2004; Wilcox et al., 2006; Cahill and Lucey, 2007; Denevi et al., 2008; Cahill et al., 2009; Li and Li, 2010]. To demonstrate *Hapke's* radiative transfer theory, *Clark and Roush* [1984], *Mustard and Pieters* [1987, 1989] used laboratory datasets. *Lucey* [2004] used *Hapke's* radiative transfer model to map clinopyroxene, orthopyroxene, plagioclase, and olivine of fresh samples (optical maturity > 0.3) on the lunar surface. To improve mapping efficiency, the look up Table (LUT) was applied in his study. The abundance interval for plagioclase, olivine, clinopyroxene, and orthopyroxene was set 10%, which means accuracy is difficult to control within 10%. Additionally, in his study, agglutinate, ilmenite, and volcanic glass were not mapped. *Lawrence and Lucey* [2007] used Hapke's radiative transfer model to retrieve mineral compositions of meteoritic assemblages. They pointed out that due to spectral effects of SMFe it is difficult to determine certain metal-rich meteoroids uniquely. A similar problem occurs with lunar materials. *Cahill and Lucey* [2007] modeled the spectral classes identified by *Tompkins and Pieters* [1999] with Hapke's radiative transfer model. Mineralogy for some spectral classes can be determined uniquely. However, for some pyroxene-rich classes, the mineralogic solutions are ambiguous. In this study, mineral end-members were set as plagioclase, olivine, orthopyroxene, and clinopyroxene. Look up Table was used to invert their radiative transfer model and mineral volume intervals were set as 5%. *Denevi et al.* [2008] demonstrated

Hapke's radiative transfer theory through modeling the near-infrared spectra of lunar mare soils. In their model, particle size, SMFe, and all dominant minerals on lunar surface (agglutinate, pyroxene, plagioclase, olivine, ilmenite and volcanic glass) were taken into account. However, spectra of agglutinate were considered to lack any absorption features, which is not consistent with spectra measured in laboratory (e.g., spectrum AG-CMP-001 from RELAB). Because of this false assumption there are significant differences between modeled and measured mineral compositions of Apollo samples [*Denevi et al., 2008*]. *Cahill et al.* [2009] investigated the compositional variations of the lunar curst through modeling central peak spectra with a radiative transfer model. In their model, mineral modes were set as plagioclase, olivine, orthopyroxene, and clinopyroxene. Look up Table technology was used. The mineral volume interval was set 5%. With this model, they had problems in identifying ferroan and magnesian anorthositic material near the crust-mantle boundary of the Feldspathic Highlands Terrane. Thus, accuracy of radiative transfer models in these studies is constrained by lacking of dominant minerals in their model and by look up Table technique.

In summary, GM, MGM, MLR, PCR, PLS, GA-PLS, ANN, and SMA have their limitations compared with RTM. So, in our project, we will extend Hapke's RTM based on previous studies in following aspects: first, all lunar surface dominant minerals will be put together as the mineral end-members;

second, spectral effects of temperature and topography will be taken into account; third, when retrieving the imaginary coefficient of minerals' optical constants and doing inversion RTM, Newton's theory for solving non-linear equation(s) will be used instead of commonly used look up Table. Our extended RTM will be then used to do lunar global mineral mapping and lunar regolith physical properties analyses.

III. DATA

3.1. Lunar soil characterization consortium (LSCC)

The LSCC dataset was used to test our forward and inverse RTM. The LSCC dataset including 9 mare and 10 highland samples were developed by *Taylor et al.* [1999, 2000, 2003, 2010], which is the only complete 'ground truth' data of the Moon consisting both soil reflectance spectra and mineral abundances. Each sample has four particle size groups (< 10 μm, 10 - 20 μm, 20 - 45 μm, < 45 μm). For the particle size groups < 10 μm, 10 - 20 μm and 20 - 45 μm, spectral reflectance in the range of 300 - 2600 nm, the corresponding modal mineral abundance as well as chemistry and Is/FeO were measured, while for the bulk soils < 45 μm the modal mineral abundance was not available. Spectra were resampled to the Clementine resolution: 415 nm, 750 nm, 900 nm, 950 nm, 1000 nm, 1100 nm, 1250 nm, 1500 nm, 2000 nm. The reflectance spectra were measured in RELAB at Brown University with the following viewing geometry: incidence angle 30^0, emittance angle 0^0 and phase angle 30^0 [e.g., *Tayor et al., 1999*]. The samples in the 10 - 20 μm group were used in the forward RTM because the reflectance of this size group is consistent with the bulk soil reflectance and all samples in the LSCC dataset were tested with the inverse RTM.

3.2. Mineral endmembers

In this study, the reflectance spectra of mineral end-members were acquired from the USGS mineral library and RELAB at Brown University (Table 1). If more than one spectra is used for an end-member, the average values of k (imaginary part of the optical constant) derived from these spectra will be used as this end-member's absorption coefficients. If the endmember mineral is separated from Apollo samples, its spectra have the highest priority compared with others. The spectra of agglutinate, plagioclase, ilmenite, olivine, metallic iron and volcanic glasses (the black and orange glasses) are selected from RELAB at Brown University, whereas the spectra of orthopyroxene (three spectra are used) and clinopyroxene come from the USGS mineral library. Their reflectance spectra are shown in Figure 1.

Table 1. The reflectance spectra of all mineral endmembers used in this study.

Mineral	Spectra Label	Size Range (μm)	Size used (μm)	Reference
Agglutinate	LU-CMP-007-1	100 - 1000	110	RELAB
Clinopyroxene	Augite WS592	400 (average)	400	USGS
Orthopyroxene	Enstatite NMNH128288	25 (average)	25	USGS
	Hypersthene PYX02.A	10 - 20	15	
	Bronzite HS9.3B	260 (average)	260	
Olivine	LR-CMP-014	0 - 45	20	RELAB
Ilmenite	MR-MSR-006	0 - 20	15	RELAB
Plagioclase	LS-CMP-086	0 - 20	11	RELAB
Metallic Iron	SA-JBA-024	0 - 1000	1	RELAB
Volcanic Glass	DD-MDD-030 (black glass)	0 - 50	10	RELAB
	LR-CMP-051 (orange glass)	-	10	

IV. METHODS

4.1. Radiative transfer modeling

4.1.1. Parameterization of the Hapke model

Several terms in the Hapke model shown as equation 2 need to be parameterized. In this implementation, the viewing geometry is set as: $e = 0^0$, $i = 30^0, g = 30^0$; $B(g)$ is approximated $B(g) = \frac{1}{1 + (1/h)\tan(g/2)}$ at 3% error, where h is the angular-width parameter of opposition effect and approximated by $h = -\frac{3}{8}\ln(1-\phi)$ with the filling factor ϕ is set to be 0.41 for the lunar regolith [*Bowell et al., 1989*]; the phase function $P(g)$ is written as $P(g) = 1 + bP_1(g) + cP_2(g)$, where $P_1(g) = \cos g$ and $P_2(g) = \frac{3}{2}\cos^2 g - \frac{1}{2}$ are Legendre polynomials and b and c are set as -0.4 and 0.25, respectively for forward scattering of minerals [*Mustard and Pieters, 1989*]; the H function is approximated within 1% error using an equation proposed by *Hapke* [2005], i.e. $H(x,y) = \left\{1 - (1-\gamma)x\left[r_0 + \left(1 - \tfrac{1}{2}r_0 - r_0 x\right)\ln\left(\tfrac{(1+x)}{x}\right)\right]\right\}^{-1}$, where x is the cosine of the emission angle or the incident angle, y is the average single scattering albedo (SSA) and $\gamma = \sqrt{1-y}$, $r_0 = \frac{1-\gamma}{1+\gamma}$.

4.1.2. Deriving SSA (ω) of individual mineral end-members from its optical constants

The average single scattering albedo (SSA, ω_{ave}) of a sample needs to be derived from the SSA of each mineral endmember. The SSA of a mineral depends on the optical constant and grain size of each mineral, and an expression for computing mineral SSA has been given by *Hapke* [2005].

$$\omega = s_e + (1 - s_e)\frac{(1 - s_i)\Theta}{1 - s_i\Theta} \quad (11)$$

$$s_e = \frac{(n-1)^2 + k^2}{(n+1)^2 + k^2} + 0.05 \quad (12)$$

$$s_i = 1 - \frac{4}{n(n+1)^2} \quad (13)$$

$$\Theta = e^{-\alpha\langle D\rangle} \quad (14)$$

where s_e is the Fresnel reflectivity for externally incident light, s_i is the Fresnel reflectivity for internally incident light, n is the real part of refraction index of a mineral, and k is the imaginary part of refraction index of the mineral; Θ is the internal-transmission coefficient of the particle without internal scatters, $\langle D\rangle$ is the average distance traveled by transmitted rays during one traverse of a particle and α is the absorption coefficient of the mineral.

Laboratory measured n values for all minerals (plagioclase, clinopyroxene, orthopyroxene, olivine, ilmenite, agglutinate, metallic iron, volcanic glass) of interest in this study are adopted from published literature and listed in Table 2, $\langle D \rangle$ can be calculated as: $\langle D \rangle = \frac{2}{3}\left(n^2 - \frac{1}{n}\left(n^2 - 1\right)^{\frac{3}{2}} \right) D$ for perfectly spherical particles [*Hapke, 2005*], $\langle D \rangle = 0.2D$ for irregular particles [*Shkuratov and Grynko, 2005*], D is the particle size, and $\alpha = \frac{4\pi nk}{\lambda}$. When equations 12, 13 and 14 are inserted into equation 11, which is then insert equation 10 for a single mineral, a nonlinear relationship between reflectance and k can be created for the mineral. Therefore the reflectance spectrum of a mineral at a specified particle size can be reproduced when its optical constants n and k of are known; and on the other hand k of this mineral can be inversed from the reflectance spectrum when the particle size and n for this mineral are specified. However, deriving k from the reflectance spectrum of a mineral is not straightforward even if n and particle size of the mineral are known.

Table 2. Refractive indices of all mineral endmembers used in this study.

Mineral	Refractive Index (*n*)	Reference
Agglutinate	1.49	*Bell et al., 1976*
Clinopyroxene	1.73	*Lucey, 1998*
Orthopyroxene	1.77	*Lucey, 1998*
Olivine	1.83	*Lucey, 1998*
Ilmenite	2.13	*Johnson and Christy, 1974*
Plagioclase	1.56	*Egan and Hilgeman, 1975*
Metallic Iron	2.25 - 3.36	*Johnson and Christy, 1974*
Volcanic Glass	1.64	*Masson et al., 1972*

4.1.3. Accommodating spectral effects of space weathering

Space weathering on the lunar surface can lead to three important changes: increasing the abundance of SMFe and agglutinate, decreasing the particle size of lunar surface materials. The SMFe makes the reflectance spectrum reddening, darker, and subdued absorption bands [*Heiken et al., 1991; Lucey et al., 1995; Starukhina and Shkuratov, 2001; Noble et al., 2001; Taylor et al., 2010*]. The agglutinate makes the reflectance spectrum subdued absorption bands [*Heiken et al., 1991; Taylor et al., 2003, 2010*]. The particle size of materials has a negative relationship to their reflectance intensity [*Mackey et al., 1974; Noble et al., 2001; Starukhina and Shkuratov, 2001; Taylor et al., 2003, 2010*].

To accommodate the spectral effect of space weathering, *Hapke* [2001] proposed to use a modified absorption coefficient of any host materials containing SMFe.

$$\alpha = \frac{4\pi n_h k_h}{\lambda} + \frac{36\pi z M_{Fe} \rho_h}{\lambda \rho_{Fe}} \qquad (15)$$

where n_h, k_h, ρ_h are refraction indices, absorption coefficients and densities of host materials, respectively; similarly $n_{Fe}, k_{Fe}, \rho_{Fe}$ are refraction indices, absorption coefficients and densities of SMFe, respectively; λ is wavelength; M_{Fe} is the mass fraction of SMFe; z is expressed in the form of the following:

$$z = \frac{n_h^3 n_{Fe} k_{Fe}}{\left(n_{Fe}^2 - k_{Fe}^2 + 2n_h^2\right)^2 + 4n_{Fe}^2 k_{Fe}^2} \qquad (16)$$

4.1.4. Accommodating temperature and topography spectral effects

Both temperature and topography have effects on lunar reflectance. Temperature on the lunar surface can reach 400 k which enables fast molecular vibration and emission of long wavelength radiation especially in the wavelength region longer than 2000 nm [e.g., *Hinrichs and Lucey, 2002; Clark et al., 2009; Li and Li, 2010*]. Lunar surface reflectance also varies with local surface normal directions because of topography. In order to accommodate the spectral effect of the rough surface on the Moon and other planets, *Hapke* [1984] defined reflectance for a rough lunar surface:

$$R_{tot} = R * E_r + R_T \qquad (17)$$

R_{tot} is the bidirectional reflectance spectrum from the lunar surface; R is the bidirectional reflectance spectrum from the flat lunar surface; E_r is used to describe the spectral effect of topography; R_T is the spectral effects of temperature defined as the ratio of the radiance (I_s) emerging from samples surface to the irradiance of illuminating target samples (J) [*Hapke, 2005*].

The contribution of the temperature effect to the lunar surface reflectance due to thermal radiation of the Moon is described by Plank's law, and radiance at a uniform temperature T can be computed with equation 13.21 in *Hapke* [2005].

$$I_s = \frac{\gamma}{\pi} H(\mu) U(\lambda, T) \qquad (18)$$

Where $U(\lambda, T)$ is the Plank function, $U(\lambda, T) = \frac{2\pi h_0 c_0^2}{\lambda^5} \frac{1}{e^{h_0 c_0 / \lambda k_0 T}}$; h_0 is Planck's constant ($h_0 = 6.626 \times 10^{-34} J \sec$); c_0 is the speed of light; k_0 is Boltzmann's constant ($k_0 = 1.381 \times 10^{-23} JK^{-1}$).

Given the irradiance of illuminating target samples (J), the thermal radiance can be transformed into the bidirectional reflectance in a form of:

$$R_T = \frac{I_s}{J} \qquad (19)$$

If reflectance spectra are measured in the laboratory, the value of J equals the irradiance of the light source at the distance of the samples from the light.

Because the thermal radiation from the lunar surface is captured simultaneously along with the reflected light by spacecraft sensors, R_T should be compensated before the reflectance data are used for spectrally modeling lunar composition.

For the lunar topography and the specified illumination geometry ($i = 30^0$, $e = 0^0$), *Hapke* [2005] gave an expression for E_r as equation 12.54. There is a parameter for the measurement of topography $\bar{\theta}$ that is the mean slope angle of the lunar surface depending on the angular resolution of the detector and the physics of the radiative transfer equation [*Hapke, 2005*]; this parameter can be specified with data from the Lunar Orbiter Altimeter (LOLA) on board the Lunar Reconnaissance Orbiter (LRO).

4.2. Application of the Newton's method in forward and inverse radiative transfer model

4.2.1. Deriving the imaginary part (k) of optical constants

We propose to derived k from the reflectance spectrum of a mineral endmember by solving the non-linear equation between the reflectance spectrum of a mineral endmember (R) and k using the Newton's method [e.g., *Kelley, 2003*]. This equation is derived by first generating the nonlinear relationship between R and k inserting equations (12), (13) and (14) with $\alpha = \frac{4\pi nk}{\lambda}$ and <D>

to (11), and equation (11) to (10) and then constructing the nonlinear equation: $F(k) = R(k) - R_{measured} = 0$ because our target is to use the non-linear relation between R and k to approximate the measured reflectance spectrum of a mineral, i. e. $R(k) = R_{measured}$. The solution k' can be determined by:

(1) Let k_i be an initial approximation to k';

(2) Calculate $F'(k_i)h + F(k_i) = 0$, where h is the gradient;

(3) $\varepsilon(k_i) = F(k_i)$, ε is the residual;

(4) Set $k_{i+1} = k_i + h$, where i = 0, 1, 2...; and k' would be the k_i value minimizing ε.

To derive k for mineral endmembers adopted from the USGS mineral library or RELAB at Brown University (described in section 3.2), particle size needs to be specified. Because the particle size presented in Table 1 for each mineral endmember has a wide range, approximate values of these ranges are used in this study. Based on anti-weathering ability for all the endmember minerals, the particle size of agglutinate, plagioclase and volcanic glass is set close to the lowest limitation of their particle size range (Table 1), with the particle size of the rest endmembers being close to the highest limitation (Table 1) [*Pieters et al., 2003*]. k for all the mineral endmembers used ranges from 0 to 0.1 in the VIS-NIR region [e.g., *Luecy, 1998; Denevi et al. 2008*]. k for iron is generally larger than 1 [e.g., *Yolken and Kruger, 1965; Johnson and Christy,*

1974]. Therefore, iterations are set for k to vary from 0 - 0.1 for minerals and for iron, k is allowed to vary from 0 to 10. When ε is minimized, k is thought to be the solution of this equation. For each mineral endmember, the k values in the VIS-NIR regions is derived in this way and shown in Figure 4. With known *n* and k, the forward and inverse models are ready to run [e.g., *Clark and Roush, 1984; Mustard and Pieters, 1987; Clark et al., 2001; Lucy, 2004; Lawrence and Lucey, 2007; Denevi et al., 2008*].

What should be noted is that when k > 0.1, the application of the above steps to derive k values will result in errors [e. g., *Hapke, 2001; Lawrence and Lucey, 2007*]. This may the reason why our derived k values of iron (our optical constants are in the form $m = n(1 + ik)$) have a trend higher in the visible region and lower in the near infrared region than values reported by *Johnson and Christy* (1974). Yet, derived k values for iron is lower than those reported by *Yolken and Kruger* (1965).

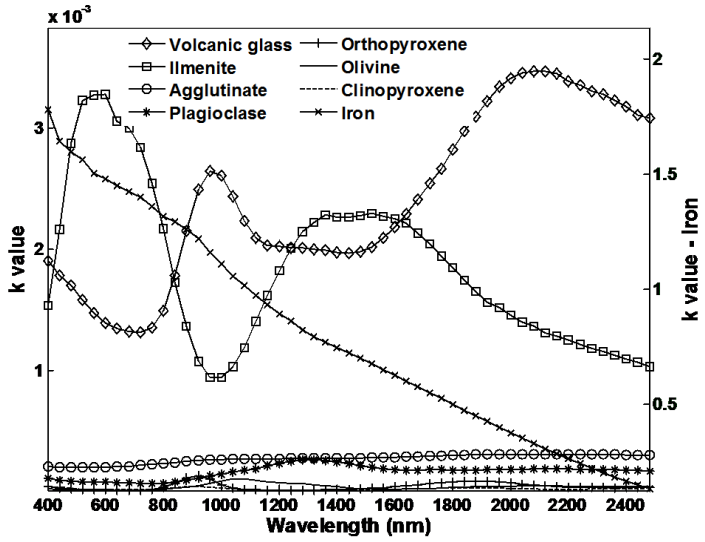

Figure 4. k values for all mineral endmembers used in the study, k values for orthopyroxene are the averaged k of three orthopyroxene samples and k values for volcanic glass is the average of the two samples listed in Table 1.

4.2.2. Deriving mineral abundance, particle size and SMFe

After initial parameterization, four parameters of the training samples required to run the inverse radiative transfer model are their reflectance spectra, particle size, abundances of minerals and SMFe. The spectra and mineral abundances are provided by the LSCC dataset. The inverse radiative transfer model implemented here can be used to derive particle size and the abundance of SMFe if the reflectance spectra and the abundance of minerals are known. On the

other hand, if particle sizes, the abundance of SMFe, and the reflectance spectra are given, the abundances of minerals of interest can be estimated.

To derive the particle size and the abundance of SMFe, equation 10 can be used to establish non-linear equations ($F(ps, M_{Fe})$) at different wavelengths describing the dependence of the bidirectional reflectance on particle size and the abundance of SMFe:

$$\varepsilon_{\lambda_j}(ps, M_{Fe}) = F_{\lambda_j}(ps, M_{Fe}) \qquad (20)$$

Where $F_{\lambda_j}(ps, M_{Fe})$ is the nonlinear equation with variables reflectance (R), the particle sizes (ps) and the abundance of SMFe (M_{Fe}) at the wavelengths λ_j.

An iteration is set in the inverse radiative transfer model to make M_{Fe} and ps change within their range until $\varepsilon(ps, M_{Fe})^2$ is minimized (equation 21), based on that each particle size group of the LSCC dataset has a specified size range (Table 1), and the abundance of SMFe with a range 0 - 1% (wt. %) [*Morris et al., 1978*]. The resultant ps and M_{Fe} from the iteration are the solutions of these non-linear equations.

$$\min(\varepsilon(ps, M_{Fe})^2) = \min(\varepsilon_{\lambda_1}(ps, M_{Fe})^2 + \varepsilon_{\lambda_2}(ps, M_{Fe})^2 + \bullet\ \bullet\ \bullet + \varepsilon_{\lambda_n}(ps, M_{Fe})^2) \qquad (14)$$

where n is the number of spectral bands.

To derive the abundances of minerals of interest, a similar process to that for deriving the particle sizes and the abundance of SMFe is repeated, but nonlinear equations need to be set for the unknown variable mineral abundance.

4.3. Model evaluation

To evaluate the result from forward modeling, the correlation coefficient (r) and root mean square error (RMSE) between modeled ($\hat{y}$) and measured (y) reflectance spectra are used. The correlation coefficient (r) between two spectra is calculated as:

$$r = \frac{\sum\left(y_i - \bar{y}\right)\left(\hat{y}_i - \bar{\hat{y}}\right)}{(n-1)} \qquad (22)$$

$\bar{y}$ is the mean of a measured spectrum y, and $\bar{\hat{y}}$ is the mean of a modeled spectrum $\hat{y}$, and n is the number of wavelengths. RMSE between measured and modeled spectra is defined as:

$$RMSE = \sqrt{\frac{\sum\left(\hat{y}_i - y_i\right)^2}{n-1}} \qquad (23)$$

To evaluate the result from inverse radiative transfer model, the coefficient of determination (R-squared value) and RMSE for derived mineral abundance and the correlation coefficient between measured and modeled

reflectance spectra are used. However, calculating RMSE for the inverse result uses measured and inverted compositional abundances differing from RMSE computed for forward modeling. R-squared (R^2) values are calculated as:

$$R^2 = 1 - \frac{SS_{total}}{SS_{error}} \qquad (24)$$

where: $SS_{total} = \sum_n \left(y_i - \bar{y} \right)^2$ is the variance of measured values,

$SS_{error} = \sum_n \left(\widehat{y_i} - y_i \right)^2$ is the residual sum of squares, and n is the number of samples.

V. RESULTS AND DISCUSSION

5.1. Forward RTM

The forward RTM was used to reproduce the bidirectional reflectance spectra of samples from the 10 - 20 μm group of the LSCC dataset. The use of this size group samples was based on the consideration that this particle size group has dominant spectral effect over other particle size groups on the bulk spectral property of lunar soils [*Pieters et al., 1993a*].

Among three groups of the parameters that were fed into the forward RTM, the mineral abundance is known, and particle size and SMFe are set to be dependent variables (see section 4.2.2). To obtain the best curve fit (e.g., when the residual ε is minimized), the particle size and the abundance of SMFe are allowed to float with the smallest gradient 10^{-12}. Given the fact that the LSCC dataset was measured in the laboratory, the spectral effect of topography cannot be assessed and temperature in the model was set as 300 K (the room temperature, because the LSCC spectra were measured in room temperature).

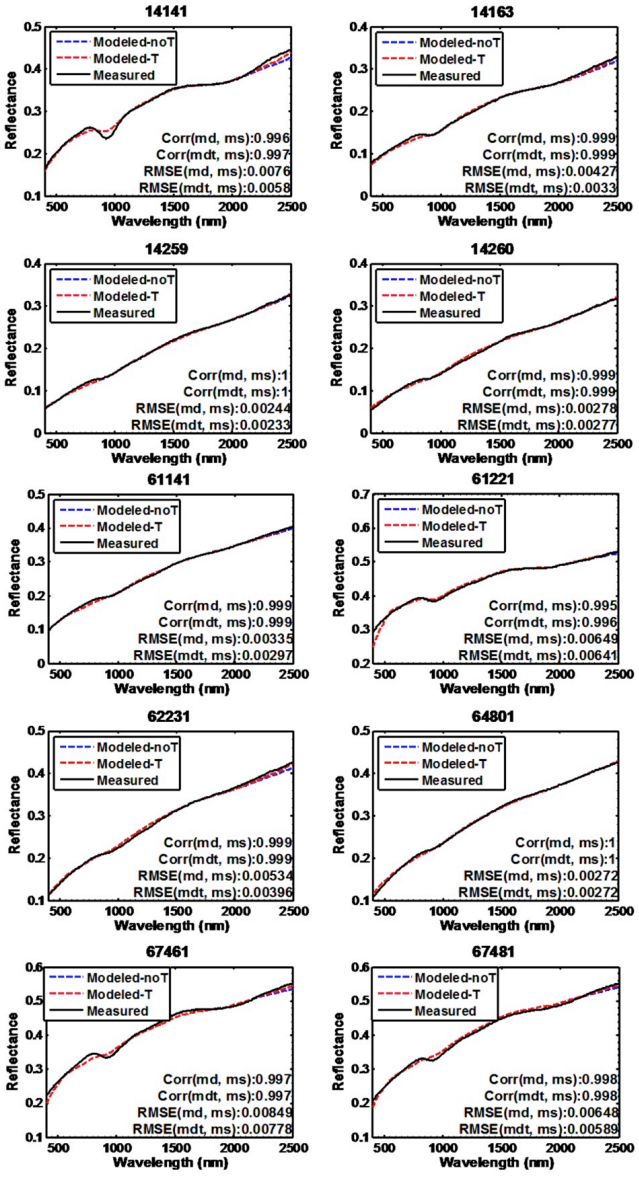

Figure 5. Comparisons between modeled (md) and measured (ms) spectra of the LSCC highland samples where corr stands for correlation coefficients and mdt indicates the modeled spectral for which temperature is considered.

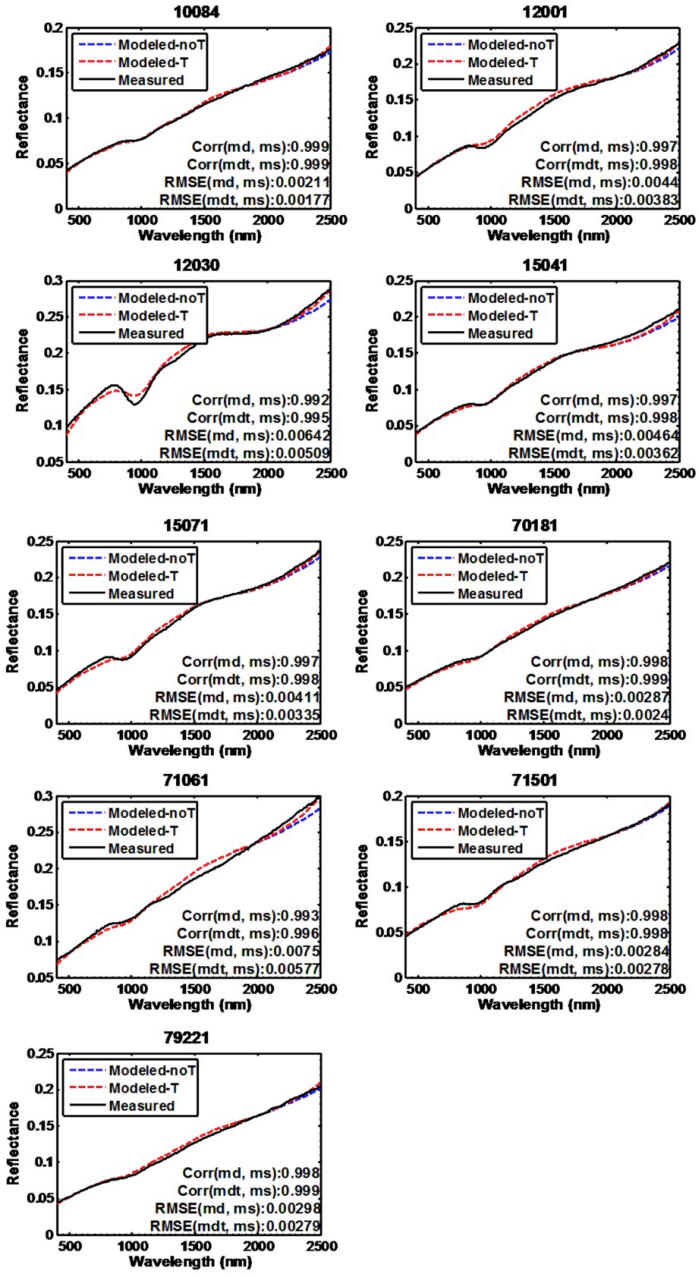

Figure 6. Comparisons of modeled (md) with measured (ms) reflectance spectra of the lunar mare samples where corr stands for correlation coefficients.

Figures 5 and 6 show the comparison between measured and modeled LSCC spectra for the highland and mare samples respectively. For the highland samples, the correlation coefficients between measured and model spectra all are larger than 0.99 indicating the high performance of the forward model. The largest RMSE values were generated for sample 67461, i.e. 0.00778 and 0.00849 when temperature was included and excluded in the model respectively. In addition, the fit for sample 14141 shows a large error (RMSE = 0.0076) when temperature was excluded. For the mare samples, the resultant correlation coefficients between measured and modeled spectra all are over 0.99. The largest RMSE value is 0.0075 for sample 71061 when the temperature effect is excluded. The spectrum of sample 71061 exhibits an unusual absorption band at 1700 nm, and this was also shown by *Denevi et al.* [2008]. However, interpretation for the presence of this absorption is currently unavailable and needs further modeling work. The fit for sample 12030 shows a similar result to that for sample 14141 (i.e. that the fitting curves for both samples show weaker absorption than measured at wavelength 950 nm). Overall the curve fitting results presented here show significant improvements as compared to those *Denevi et al.* [2008] and *Cahill et al.* [2010], which can be attributed to the use of two additional end-members: agglutinate and volcanic glasses. As expected, all fitted curved show

insignificant effects of room temperature (Figures 5 and 6), but a better fit can be obtained when this effect is considered.

As mentioned above, among the all sample spectra that are fitted, the fit for samples 12030 and 14141was poor at wavelength 950 nm. This is attributed to the use of the mean optical constants for the endmember spectra. To confirm this, an orthopyroxene spectrum with deeper absorption at 1000 nm was used to replace with the original endmember for orthopyroxene, and a much better curve fit was obtained at around 1000 nm for samples 12030 and 14141 as shown in Figure 7. For sample 12030, the correlation coefficient between measured and modeled spectra without considering the temperature effect is improved from 0.992 to 0.998, and RMSE decreases from 0.00642 to 0.00289. The modeled results for sample14141 show similar improvements: the correlation coefficient increases from 0.996 to 0.999 and RMSE decreases from 0.0058 to 0.00303.

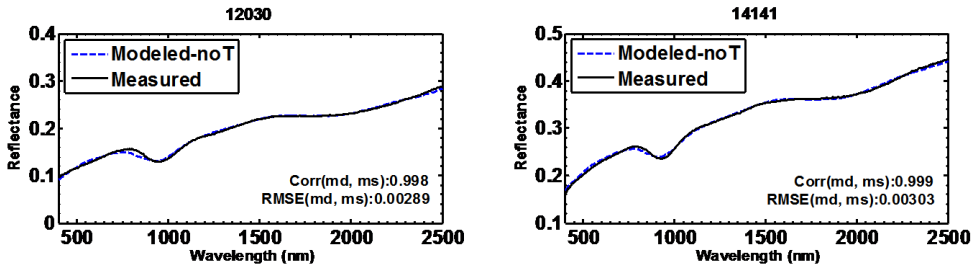

Figure 7. Comparisons of modeled (md) with measured (ms) reflectance spectra of 14141 and 12030 with new k values derived from a different orthopyroxene spectrum; and corr stands for correlation coefficient.

5.2. Inverse RTM

5.2.1. Estimated SMFe and particle size

Evaluation of the inverse result for SMFe was conducted by examining the coefficient of determination between modeled SMFe vs. measured Is/FeO, because data for lab measured metallic iron are not available from the LSCC dataset. Figure 8 shows the correlation between estimated SMFe and Is/FeO for the samples of three different particle size groups (< 10, 10 - 20, and 20 - 45 μm) of the LSCC dataset. The estimated SMFe and measured Is/FeO show a linear correlation, but the linear trend for the highland samples is different from that for the mare samples with the latter being more than twice as steep as the slope for the highland samples. This observation is consistent with the observation that soil having high FeO content accumulates metallic iron faster during the FeO reduction process than soil having low FeO content [*Morris, 1980*]. One may wonder whether normalizing Is with FeO could be responsible for this difference because mare sample have higher FeO abundance than highland soil samples. To compare Is and SMFe directly, Is was calculated by multiplying Is/FeO by the percentage of FeO in the Apollo samples. Figure 9 shows strong linear correlations between Is and the estimated SMFe. However, the slope of the linear trend for the LSCC mare samples is still larger than that for the highland samples

(the ratio of their slopes is about 1.8). Thus the slope difference between the highland and mare samples is not caused by the FeO normalization.

In *Morris* [1980], the linear relationship between the abundance of reduced metallic iron (< 33 nm in size) and measured Is: $Fe^0 = 3.2 \times 10^{-4} Is$ was given. When increasing the amount of Fe^0 with the particle size larger than 33 nm, the coefficient of this relationship will increase. Our results indicate that the modeled relation between the abundance of metallic iron and measured Is for the highland samples $Fe^0 = 3.1 \times 10^{-4} Is$ is almost the same as in *Morris* [1980], while for the mare samples as mentioned above is different: $Fe^0 = 5.6 \times 10^{-4} Is$. This may originate from the inclusion of more abundant SMFe with large particle size (e.g., > 33 nm) in the mare samples than in the highland samples. These kinds of SMFe have several sources such as bedrock and micrometeorites [*Morris, 1980*].

Morris [1980] also mentioned that in the lunar highland regions the maximum concentration of metallic iron was about 0.7% (wt. %) and in the lunar mare region the maximum abundance of metallic SMFe was about 1% (wt. %). From Figures 8 and 9, our modeled maximum concentration of iron for the highland samples is about 0. 5 % (wt. %) and for the mare samples is about 1% (wt. %).

The result for estimating SMFe presented here is compared with those in *Denevi et al.* [2008] where only the mare samples with particle size 10 - 20 μm

were used, indicating that the scatter plots of modeled SMFe vs. the Is/FeO values resulting from this study are tighter than those shown in *Denevi et al.* [2008]. This may result from the use of Newton's method and least squares for solving non-linear equations rather than the LUT method used by *Denevi et al.* [2008] because our approach can allow a gradient as small as 10^{-12}.

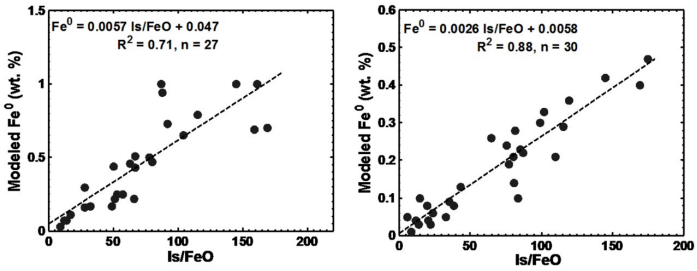

Figure 8. Comparison between Is/FeO and the abundance of SMFe derived with the inverse RTM for the LSCC mare samples (left) and highland samples (right).

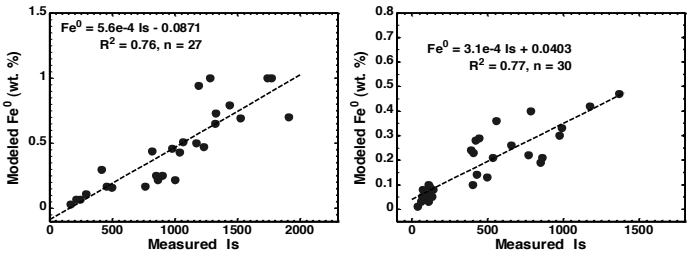

Figure 9. Comparison between Is and the abundance of SMFe derived with the inverse RTM for the LSCC mare (left) and highland (right) samples.

Figure 10 shows the estimated particle sizes for the samples of three different particle size groups in the LSCC dataset. The estimated sizes are within their measured ranges. Derivation of lunar soil particle size has not been reported in previous RTM studies.

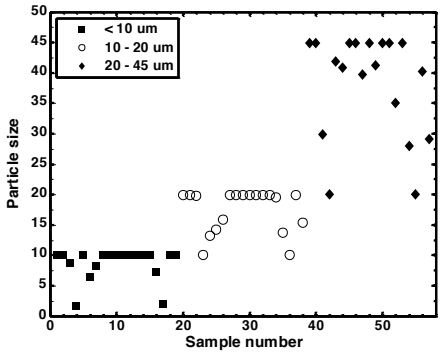

Figure 10. Derived particle sizes for the three particle size group samples of the LSCC dataset.

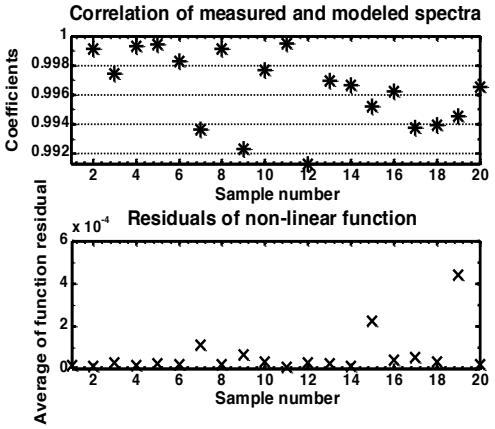

Figure 11. Correlation coefficients (up plot) between modeled and measured spectra and residuals (lower plot) of different samples derived with the inversed model.

5.2.2. Estimated mineral abundance

With the estimated particle size and SMFe, the abundances of all minerals can be derived from the reflectance spectra. The inverse RTM was first applied to all LSCC samples, and resulted in non-unique solutions to the non-linear equations. This non-unique solution was observed more for mature samples than relatively less mature samples (e.g., Is/FeO <= 60, optical maturity > 0.3). Therefore the estimation of the mineral abundance through the inverse RTM started from the freshest sample, and a mature sample was added to the testing

sample pool until a degraded correlation was produced (e.g., R^2 decreases by 0.1). With this strategy, it was found that the current RTM only works well for samples with Is/FeO <= 65 of the LSCC dataset. *Morris* [1976] grouped samples with Is/FeO larger than 60 into mature samples. Therefore almost all of our testing samples are fresh or immature. The discussion below will be focused on the 20 LSCC samples with Is/FeO equal to or less than 65.

Two plots in Figure 11 shows the correlation coefficient and residual (see how ε is calculated in section 4.2.2.) between measured spectra and modeled by the inverse RTM, and all fitting spectra are highly correlated to measured (correlation coefficients > 0.99). The largest residual for solving all the non-linear equations is less than 5×10^{-4}, and most of these residuals (18 out of 20) are less than 2×10^{-4}.

Shown in Figure 12 are comparisons between the modeled and measured mineral abundances. Table 3 shows the R^2 values between modeled and measured mineral abundances of the 20 LSCC samples. Although the abundances of clinopyroxene and orthopyroxene were modeled separately, the sum of estimated clinopyroxene and orthopyroxene abundances was used to compare with the abundance of pyroxene in the LSCC dataset.

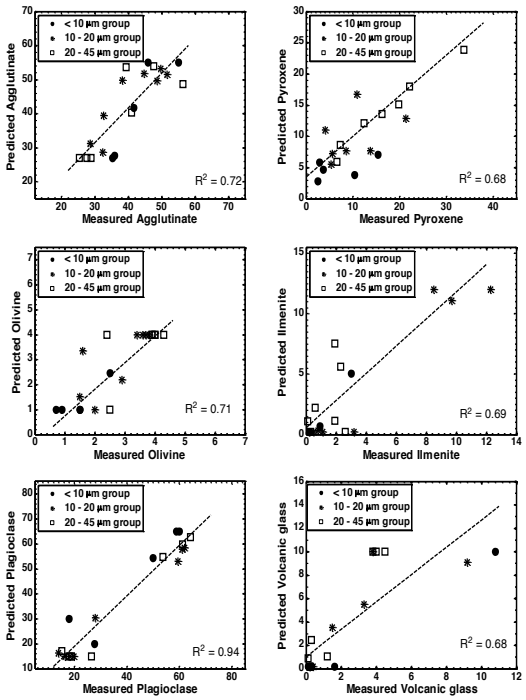

Figure 12. Correlations between measured and modeled mineral abundances derived with the inverse RTM.

Table 3. R-squared values between measured and estimated abundances of lunar minerals.

Mineral	Agglutinate	Pyroxene	Plagioclase	Olivine	Ilmenite	Volcanic glass
R^2 (< 10μm)	0.84	**0.30**	0.88	0.74	0.89	0.98
R^2 (10 - 20μm)	0.76	0.45	0.98	0.65	0.92	0.72
R^2 (20 - 45μm)	0.70	0.98	0.97	0.37	**0.14**	0.94
R^2 (three size groups)	0.72	0.68	0.94	0.71	0.69	0.68

Figure 12 and Table 3 indicate that the inverse RTM resulted in R^2 larger than 0.65 for all minerals considered with the highest correlation for plagioclase ($R^2 = 0.94$), and the lowest correlation for pyroxene ($R^2 = 0.68$). The highest accuracy for plagioclase is attributed to its unique absorption band near 1250 nm while agglutinate, olivine, and pyroxene share a common absorption band near 1000 nm resulting in a difficulty for the inverse RTM to distinguish the three minerals. The volcanic glasses on the lunar surface show large chemical variations [e.g., *Delano, 1986*], the averaged k values of two kinds of glasses were used in this study and this may degrade the estimation of volcanic glasses. The scatter plots for olivine and ilmenite are not as tight as those for the rest minerals. This relatively poor estimation may result from the inaccurate values for the optical constants (n and k) for these two mineral endmembers [e.g., *Hapke, 1981*]. One reason is that when the imaginary part of the optical constants (k) was derived, the particle size for all endmember minerals could not be well constrained (see Table 1) and the other reason is that for some mineral endmembers, the average k values of several spectra of the same type mineral samples were used (Table 1). All of these factors can lead to poor results for quantifying the abundances of endmember minerals [e.g., *Hapke, 1981; Lawrence and Lucey, 2007*].

To demonstrate how the particle size has effects on the modeling accuracy, R^2 values for individual size groups and the whole size pool are listed. The particle size shows a slight influence on estimating agglutinate, plagioclase, olivine and volcanic glass. However, estimated pyroxene and ilmenite abundances may not be independent of particle size. The performance of the inverse RTM for quantifying pyroxene degrades with decreasing the particle size, and this could be ultimately due to significantly subdued absorptions of pyroxene at 1000 nm and 2000 nm at a small particle size [*Pieters et al., 1993a*]. While for the estimation of ilmenite, larger particle sizes lead to a poor performance. Ilmenite is an opaque mineral, and spectrally featureless. Therefore smaller particle sizes could exhibit higher reflectance and relatively less subdued spectral information available for the inverse RTM.

The exact reason why the inverse model does not perform well for mature lunar samples (Is/FeO > 65) cannot be pinned down at this stage. A primary reason may be that the spectral effect of SMFe cannot be accommodated equally well across the spectral region 0.4 - 2.5 μm. For example, the Hapke radiative transfer model for accommodating the effect of SMFe showed an excellent spectral curve fit for shorter wavelengths, but the fit was relatively poor for the wavelengths longer than 1.4 μm [*Hapke, 2001*]. In this study, the derivation of SMFe is decoupled from the estimation of the mineral abundance with the former

being derived first and then fixed for the estimation of the latter by solving nonlinear equations. As a result, the abundance estimation for the mineral constituents that have a significant spectral effect beyond 1.4 μm could be penalized because adjusting the abundance of these constituents could force the model to produce a good fit. These constituents could be opaque ilmenite and/or agglutinate containing volumetrically dispersed SMFe.

VI. CONCLUSION

In our study, Hapke's radiative transfer model has been implemented so that 1) all lunar surface dominant minerals (plagioclase, clinopyroxene, orthopyroxene, olivine, ilmenite, volcanic glasses and agglutinate) are considered, 2) Newton's method and least squares are jointly used to solve non-linear equation(s) for deriving optical constants and mineral abundances, and 3) the spectral effects of temperature and topography are incorporated into the model.

The result for the forward RTM shows high correlation coefficients (> 0.99) between modeled and measured spectra for all the LSCC samples, and the largest error is only 0.00849 (sample 67461), lower than 2% of the mean reflectance spectral data for all the bands. The spectral effect of the room temperature shows a very weak contribution in the longer wavelengths (> 2000 nm) as expected. The spectral effect of topography cannot be tested though we have incorporated it into our model.

The result for the inverse RTM suggest that both lunar soil SMFe and particle size can be estimated reliably and efficiently with the use of Newton's method and least squares. The relationship of SMFe to Is for the mare samples is different from that for the highland samples, which has been attributed to the effect of more abundant SMFe with large particle size (e.g., > 30 nm) in the mare samples. The inverse RTM is also used to quantify the abundances for all the end-

member minerals. The inverse result for the LSCC samples with Is/FeO equal to or less 65 than indicates that R-squared between modeled and measured mineral abundances are all larger 0.65 with the highest for plagioclase ($R^2 = 0.94$), and the lowest for pyroxene ($R^2 = 0.68$).

It is the first attempt to consider agglutinate and volcanic glasses as mineral end-members in both forward and inverse RTM. The inverse RTM shows better performances and significant improvements over the methods used in previous studies [e.g., *Lucey, 2004; Denevi et al., 2008*]. For the future work, we should identify possible factors that lead to non-unique solutions and poor performances of the inverse RTM for modeling samples with higher maturity (Is/FeO > 65). The inverse RTM can then be used to quantify lunar surface minerals with remote sensing images (e.g., UV-VIS-NIR Clementine image, M^3 image) through incorporating the LRO temperature and topography data.

REFERENCES

Adams, J. B., and L. H. Goullaud (1978), Plagioclase feldspars: Visible and near infrared diffuse reflectance spectra as applied to remote sensing, *Proc. Lunar planet Sci. Conf. 9th*, 2901-2909.

Anand, M., L. A. Taylor, M. A. Nararov, J. Shu, H. k. Mao, and R. M. Hemley (2004), Space weathering on airless planetary bodies: Clues from the lunar mineral hapkeite, *Proceedings of the National Academy of Sciences*, *101*, 6847-6851.

Bishop, C. M. (1998), *Neural Networks for Pattern Recognition*, pp. 482, Clarendon press, Oxford.

Cahill, J. T. S., P. G. Lucey, and M. A. Wieczorek (2009), Compositional variations of the lunar crust: Results from radiative transfer modeling of central peak spectra*, J. Geophys. Res., 114,* E09001.

Cahill, J. T., and P. G. Lucey (2007), Radiative transfer modeling of lunar highlands spectral classes and relationship to lunar samples, *J. Geophys. Res., 112,* E10007.

Clark, B. E., P. G. Lucey, P. Helfenstein, J. F. Bell lii, C. Peterson, J. Veverka, and T. Mcconnochie et al. (2001), Space weathering on Eros: Constraints from albedo and spectral measurements of Psyche crater, *Meteorit. Planet. Sci., 36,* 1617-1637.

Clark, R. N. (1983), Spectral properties of mixtures of montmorillonite and dark carbon grains: implications for remote sensing minerals containing chemically and physically adsorbed water, *J. Geophys. Res., 88,* 10635-10644.

Clark, R. N., and T. L. Roush (1984), Reflectance spectroscopy: quantitative analysis techniques for remote sensing applications, *J. Geophys. Res., 89,* 6329-6340.

Combe, J. B., T. B. McCord, G. Y. Kramer, C. M. Pieters, L. A. Taylor, N. E. Petro, and J. W. Boardman et al. (2010), Mixing of surface materials investigated by spectral mixture analysis with the Moon Mineralogy Mapper, *LPSC*, abstract 2215.

Denevi, B. W., P. G. Lucey, and S. B. Sherman (2008), Radiative transfer modeling of near-infrared spectra of lunar mare soils: Theory and measurement, *J. Geophys. Res., 113,* E02003.

Dorschner, J., B. Begemann, T. Henning, C. Jaeger, and H. Mutschke (1995), Steps toward interstellar silicate mineralogy. II. Study of Mg-Fe-silicate glasses of variable composition, *Astron. Astrophys., 300,* 503-519.

Drake, M. J. (1986), *Is lunar bulk material similar to Earth's mantle? In origin of the Moon*, pp. 105-124. Lunar and planetary Institute, Houston.

Forrest, S. (1993), Genetic algorithm: Principles of natural selection applied to computation, *Science, 261,* 872-878

Geladi, P., and B. Kowaski (1986), Partial least squares regression: A tutorial, *Analytia Chimica Acta, 185,* 1-17.

Hapke, B. (1981), Bidirectional reflectance spectroscopy: I. Theory, *J. Geophys. Res.*, *86,* 3039-3054.

Hapke, B. (1984), Bidirectional reflectance spectroscopy: 3. Correction for macroscopic roughness, *Icarus*, *59,* 41-59.

Hapke, B. (1986), Bidirectional reflectance spectroscopy: 4. The extinction coefficient and the opposition effect*, Icarus*, *67,* 264-280.

Hapke, B. (2001), Space weathering from Mercury to the asteroid belt, *J. Geophys. Res.*, *106,* 10039-10073.

Hapke, B. (2005), *Theory of reflectance and emittance spectroscopy*, Cambridge University Press, New York.

Hartmann, W. K., R. J. Phillips, and G. J. Taylor (1986), *Origin of the Moon*, pp. 781, Lunar and Planetary Institute, Houston.

Heiken, G. H., T. Vaniman, and B. M. French (1991), *Lunar sourcebook: A User's Guide to the Moon,* Cambridge University Press, New York

Helfenstein, P., and J. Veverka (1998), Submillimeter-scale topography of undisturbed lunar soils, *LPSC, XXIX.*

Hiroi, T., and C. M. Pieters (1994), Estimation of grain sizes and mixing ratios of fine powder mixtures of common geologic minerals, *J. Geophys, Res., 99,* E5.

Johnson, P. M., M. O. Smith, and J. B. Adams (1992), Simple algorithms for remote determination of mineral abundances and particle sizes from reflectance spectra, *J. Geophys. Res., 97,* 2649-2657.

Jolliff, B. L. (1999), Clementine UV-VIS multispectral data and the Apollo 17 landing site: what can we tell and how well? *J. Geophys. Res., 104,* 14123-14148.

Kaula, W. M. (1971), Dynamical aspects of lunar origin, *Rev. Geophys. Space Phys., 9,* 217-238.

Korokhin, V. V., V. G. Kaydash, Y. G. Shkurakov, D. G. Stankevich, and U. Mall (2008), Prognosis of TiO2 abundance in lunar soil using a non-linear analysis of Clemetine and LSCCdata, *Planetary and Space Science, 56,* 1063-1078.

Lawrence, S. J., and P. G. Lucey (2007), Radiative transfer mixing models of meteoritic assemblages, *J. Geophys. Res., 112,* E07005.

Li, L. (2006), Partial lease squares modeling to quantify lunar soil composition with hyperspectral reflectance measurements, *J. Geophys. Res., 111*, E04002.

Li, L., and J. F. Mustard (2000), Compositional gradients across mare-highland contacts: Importance and geological implication of lateral transport, *J. Geophys, Res., 105,* E8.

Li, L., and J. F. Mustard (2003), Highland contamination in lunar mare soils: Improved mapping with multiple endmember spectral mixture analysis (MESMA), *J. Geophys, Res., 108,* E7.

Li, L., J. F. Mustard, and G. He (1996), Mixing across simple mare-highland contacts: new insights from Clementine UV-VIS data of the Grimaldi basin, *Lunar and Planetary Science XXVII,* 751-752.

Li, S., and L. Li (2010), Radiative transfer modeling of lunar soil reflectance for accommodating the effects of roughness and temperature*, LPSC*, *XXXXI*.

Lucey, P. G. (2004), Mineral maps of the Moon, *Geophysical Research Letters*, *31,* L08701.

Lucey, P. G., D. T. Blewett, and L. Li (2000), Lunar iron and titanium abundance algorithm based on final processing of Clementine ultraviolet-visible images, *J. Geophys. Res., 105,* 20297-20305.

Mckay, D. S., R. M. Fruland, and G. H. Heiken (1974), Grain size and the evolution of lunar soils, *Proceedings of the Fifth Lunar Conferrence*, 887-906.

Moroz, L., and G. Arnold (1999), Implications for remote sensing: 1. Nonlinear mixing modeling, *J. Geophys, Res., 104,* 14109-14121.

Mustard, J. F., and C. M. Pieters (1987), Quantitative abundance estimates from bidirectional reflectance measurements, in Proceedings of the 17th Lunarand Planetary Science Conference, *J. Geophys. Res.*, *92,* E617-E626.

Mustard, J. F., and C. M. Pieters (1989), Photometric phase functions of common geologic minerals and applications to quantitative analysis of mineral mixture reflectance spectra, *J. Geophys. Res., 94,* 13619-13634.

Myers, R. H. (1989), *Classical and Modern Regression with Applications (Second Edition)*, pp. 217-230, PWS-KENT Publishing Company, Boston.

Noble, S. K., C. M. Pieters, L. A. Taylor, R. V. Morris, C. C. Allen, D. S. Mckay, and L. P. Keller (2001), The optical properties of the finest fraction of lunar soil: Implications for space weathering, *Meteoritics & Planetary Science*, 36, 31-42.

Noble, S. K., C. M. Pieters, T. Hiroi, and L. A. Taylor (2006), Using the Modified Gaussian Model to extract quantitative data from lunar soils, *J. Geophys, Res., 111,* E11009.

Pieters, C. M. (1986), Composition of the lunar highland crust from near-infrared spectroscopy, *Rev. Geophys.*, 24, 557-578.

Pieters, C. M., and P. A. J. Englert (1993), *Remote Geochemical Analysis: Elemental and Mineralogical Composition,* Cambridge University Press, New York.

Pieters, C. M., D. G. Stankevich, Y. G. Shkuratov, and L. A. Taylor (2002), Statistical Analysis of the Links among Lunar Mare Soil Mineralogy, Chemistry, and Reflectance Spectra, *Icarus, 115,* 285-289.

Pieters, C. M., E. M. Fischer, O. Rode, and A. Basu (1993b) Optical effects of space weathering: The role of the finest fraction, *J. Geophys. Res., 98,* 20817-20824.

Pieters, C. M., J. W. Head, and J. M. Sunshine et al. (1993a), Crustal Diversity of the Moon: Compositional Analyses of Galileo Solid State Imaging Data, *J. Geophys, Res., 98,* E9.

Pieters, C. M., S. Tompkins, J. W. Head, and P. C. Hess (1997), Mineralogy of the mafic anomaly in the South Pole-Aitken Basin: Implications for excavation of the lunar mantle, *J. Geophys, Res.,* 24, 1903-1906.

Pieters, C. M., D. G. Stankevich, Y. G. Shkuratov, and L. A. Taylor (2002), Statistical analysis of the links among lunar mare soil mineralogy, chemistry and reflectance spectra, *Icarus, 155,* 285-298.

Pieters, C., Y. Shkuratov, V. Kaydash, D. Stankevich, and L. Taylor (2006), Lunar soil characterization consortium analyses: Pyroxene and maturity estimates derived from Clementine image data, *Icarus, 184,* 83-101.

Pollack, J. B., D. Hollenbach, S. Beckwith, D. P. Simonelli, T. Roush, and W. Fong (1994), Composition and radiative properties of grains in molecular clouds and accretion disks, *Astrophys. J., 421,* 615-639.

Poulet, F., and E. Erard (2004), Nonlinear spectral mixing: Quantitative analysis of laboratory mineral mixtures, *J. Geophys, Res., 109,* E02009.

Poulet, F., J. N. Cuzzi, D. P. Cruikshank, T. Roush, and C. M. Dalle Ore (2002), Comparison between the Shkuratov and Hapke Scattering Theories for Solid Planetary Surface: Application to the Surface Composition of Two Centaurs, *Icarus, 160,* 313-324.

Ripley, B. D. (1996)*, Pattern Recognition and Neural networks*, pp. 403, Cambridge University Press, New York.

Scott, A., and W. W. Duley (1996), Ultraviolet and infrared refractive indices of amorphous silicates, *Astrophys. J. Suppl., 105,* 401-405.

Shkuratov, Y. G., D. G. Stankevich, V. G. Kaydash, V. V. Omelchenko, C. M. Pieters, P. C. Pinet, and S. D. Chevrel et al. (2003), Composition of the lunar surface as will be seen from SMART-1: A simulation using Clementine data, *J. Geophys, Res., 108*, E4.

Shkuratov, Y. G., V. G. Kaydash, and C. M. Pieters (2005), Lunar Clinopyroxene and Plagioclase: Surface Distribution and Composition, *Solar System Research, 39*, 255-266.

Solomon, S. C., and J. Longhi (1977), Magma oceanography: 1. Thermal evolution, *Proc. Lunar Sci. Conf.* 8th, 583-599.

Starukhina, L. V., and Y. G. Shkuratov (2001), A Theoretical Model of Lunar Optical Maturation: Effects of Submicroscopic Reduced Iron and Particle Size Variations, *ICARUS*, 152, 275-281.

Sunshine, J. M., and C. Pieters (1993), Estimating Modal Abundances From the Spectra of Natural and Laboratory Pyroxene Mixtures Using the Modified Gaussian Model, *J. Geophys, Res., 98,* E5.

Sunshine, J. M., C. M. Pieters, and S. F. Prait (1990), Deconvolution of Mineral Absorption Bands: An Improved Approach, *J. Geophys, Res., 95.* B5.

Tanton, L. T. E., J. A. V. Orman, B. H. Hager, and T. L. Grove (2002), Re-examination of the lunar magma ocean cumulate overturn hypothesis: melting or mixing is required, *Earth and Planetary Science Letters*, 196, 239-249.

Taylor, L. A., C. Pieters, A. Patchen, D. S. Taylor, R. V. Morris, L. P. Keller, and D. S. Mckay (2003), Mineralogical Characterization of Lunar Highland Soils, *LPSC*, XXXIV, abstract 1774.

Taylor, L. A., C. Pieters, A. Patchen, D. S. Taylor, R. V. Morris, L. P. Keller, and D. S. Mckay (2010), Mineralogical and chemical characterization of lunar highland soils: Insights into the space weathering of soils on airless bodies, *J. Geophys, Res., 115*, E02002.

Taylor, S. R. (1979), Structure and evolution of the Moon, *Nature, 281*, 105-110.

Tompkins, S., and C. M. Pieters (1999), Mineralogy of the lunar crust: Results from Clementine, *Meteoritic & Planetary Science*, 34, 25-41.

Tsuboi, N., S. Sugita, T. Hiroi, k. Nagata, and M. Okada (2010), A new modified Gaussian model (MGM) using the cross - validation method, *LPSC*, abstract 1744.

Warren, P. H. (1985), The magma ocean concept and lunar evolution, *Ann. Rev. Earth Planet. Sci., 13,* 201-240.

Warren, P. H. (1990), Lunar anorthosites and the magma-ocean plagioclase-flotation hypothesis: Importance of FeO enrichment in the parent magma, *American Mineralogist*, 75, 46-58.

Wilcox, B. B., P. G. Lucey, and B. R. Hawke (2006), Radiative transfer modeling of compositions of lunar pyroclastic deposits*, J. Geophys, Res., 111*, E09001.

Wood, J. A. (1975), Lunar petrogenesis in a well-stirred magma ocean, *Proc. Lunar. Sci. Conf.,* 6th, 1087-1102.

CURRICULUM VITAE

Shuai Li

Education

- M.S. *Geology*, Indiana University, IN, USA, Sep. 2009-Nov. 2011
- M.S. *Remote Sensing*, Institute of Remote Sensing Applications Chinese Academy of Sciences, Beijing, China, Sep. 2007-Jul. 2009
- B.S., *Geology*, Nanjing University, Nanjing, China, Sep. 2003-Jul. 2007

Conference Papers, Presentations and Publications

1. Li, S., and L. Li (2011), Radiative transfer modeling for quantifying lunar surface minerals, particle sizes and submicroscopic iron (SMFe), *Journal of Geophysical Research*, *116*, E09001.
2. Wang F., Q. Z. Lin, Q. J. Wang, and S. Li (2011), The study of the spectrum pre-processing method when applying the characteristic spectrum linear inversion modeling (CSLM) to extract the mineral information, *Spectroscopy and Spectral Analysis,* 31 (05).
3. Li, S., and L. Li (2010), Radiative transfer modeling for quantifying lunar mineral abundance, *AGU 2010 fall meeting*.
4. Li, S., and L. Li (2010), Comparison of three different statistical methods for retrieving the lunar mineral abundance, *AGU 2010 fall meeting*.
5. Li S., and L. Li (2010), Radiative transfer modeling of lunar soil reflectance for accommodating the effects of roughness and temperature, *LPSC XXXXI*, Abstract # 2168.
6. Li L., and S. Li (2010), Deriving lunar mineral abundance maps from Clementine multispectral imagery*, LPSC XXXXI*, Abstract # 2189.
7. Li S., Q. Z. Lin, Q. J. Liu, M. F. Wang, Q. J. Wang, and Y. M. Wei (2010), A rapid quantificational identification model of minerals and its applications, *Spectroscopy and Spectral Analysis*, 30 (05): 1315-1319.
8. Wang M. F., Q. Z. Lin, S. Li, Q. J. Wang, Y. M. Wei, Y. Chen, and Q. J. Liu (2010), Mineral identification based on characteristic spectrum: a case study of core analysis of Baogutu porphyry copper deposit in Xinjiang, NW China, *Acta Petrologica Sinica*, in press.
9. Liu Q. J., Q. Z. Lin, Q. J. Wang, H. Li, and S. Li (2009), The infrared spectrum processing based on Continuum Fast Fourier Transform (CFFT), *Spectroscopy and Spectral Analysis*, 29 (12): 3279-3282.
10. Li S., and Q. Wang (2006), Crustal compositions of the Sulu ultrahigh-pressure metamorphic belt and geological implications, *the 5·20 Conference of Department of Earth Sciences of Nanjing University*, Nanjing University, Nanjing.

11. Meng L. S., S. Li, and H. B. Jiang (2005), 3 D gravity anomaly forward modeling system, *the 8th Forum Science & Art of Nanjing University*, Nanjing University, Nanjing.

Imaging

ENVI, ERDAS, ARCMAP, ARCVIEW, ARCGIS, PHOTOSHOP, CORELDRAW

Operating System

Microsoft Windows, Linux, MC OS.

Computer Language

Visual C; Visual C ++; Visual Basic; Borland C++ Builder; Mat lab; Java; C #; IDL.

Field Work Experience

- Hushan district, Nanjing, Jiangsu Province China, Jul. 2004-Sep. 2004.
- Chao Lake, Anhui Province China, Jul. 2005-Sep. 2005.

Fellowships and Grants Received

- Cyrus Tang Foundation Scholarship (0.625% of all the undergraduates), 2003-2007.
- First Rank People's Scholarship (5% of all the class students), 2003-2007.
- Third Rank People's Scholarship (15% of all the class students), 2006.
- Arts & Sciences Talent Training Grant from Ministry of Education for Academy Training (3% of all the department undergraduates), 2005-2007.

Volunteer

- Leader of Tian Jian Student Association (supported by Cyrus Tang Foundation, Chicago, USA.), Nanjing University, 2004-2006.